A Total-Field/Scattered-Field Plane-Wave Source for the FDTD Analysis of Layered Media

İlker R. Çapoğlu, *Member, IEEE*, and Glenn S. Smith, *Fellow, IEEE*

***Abstract*—A total-field/scattered-field (TF/SF) plane-wave source is developed for the finite-difference time-domain analysis of general (possibly lossy) planar layered media. A 1-D auxiliary grid is created to generate the incident field in the presence of the layered medium. Inhomogeneous plane waves are also allowed for lossless layers and narrowband excitation.**

***Index Terms*—Electromagnetic propagation in nonhomogeneous media, finite-difference time-domain (FDTD) methods.**

I. Introduction

THE finite-difference time-domain (FDTD) method has been successfully used to analyze planar layered media; however, many useful features of FDTD available for free space have not yet been sufficiently generalized for these geometries. One of these features is the efficient implementation of an *incident wave source* for receiving antenna and scattering problems. Being the central problem in any FDTD incident wave source, the a priori calculation of the incident field in the presence of the layered medium poses the main difficulty. Since the behavior of waves in a layered medium is much more complex than in free space, the exact calculation of the incident field is usually very complicated. This is true even for the simplest type of incident wave: the plane wave. The difficulty arises from the fact that, in a layered medium, the incident plane wave consists of not only the initial wavefront, but the numerous reflections from the boundaries of the layers as well.

In this paper, we present an efficient incident plane-wave source that is applicable for general layered media. For this purpose, a generalization of the total-field/scattered-field (TF/SF) formulation (also called the plane-wave injector) [1] is introduced. In this framework, a special boundary, called the TF/SF boundary or the TF/SF box, is formed in the FDTD grid, and field corrections are applied on this boundary at each FDTD time step. The corrections serve the purpose of creating and isolating an incident plane wave inside the box, and they follow directly from the values of the incident plane wave on the TF/SF boundary. These field values are obtained numerically via an auxiliary FDTD simulation, which is carried out along with the main FDTD simulation. The procedure for achieving this will be described in later sections.

A FDTD plane-wave injector for a dielectric half space can be easily constructed using the exact theoretical formula for the reflected and transmitted fields, as done in [2]. The first FDTD plane-wave injector for a nontrivial layered medium appears to have been introduced by Hsu and Carin [3]. They developed a TF/SF boundary for injecting a plane wave on a 2-D scatterer (one that is invariant in one spatial dimension) placed on an ungrounded infinite dielectric slab. In their implementation, they used the exact theoretical expression for the plane wave scattered from the ungrounded dielectric slab. In this regard, the method is strictly limited to this specific case. Furthermore, the method is only applicable when the direction of incidence is perpendicular to the axis of invariance, namely, when the incident plane wave has no variation along the axis of invariance. Recently, Yi *et al.* [4] introduced a generalization of this technique. They allowed oblique incidence with respect to the axis of invariance and removed the necessity of deriving theoretical formulas by obtaining the incident field via a 1-D auxiliary FDTD grid. Although their presentation was limited to a lossy ground, the technique is potentially applicable to any lossy layered medium. This potential had been partially recognized by Winton *et al.* [5]. They introduced a plane-wave injector for a general lossy layered medium using the aforementioned 1-D-auxiliary-grid technique. However, their analysis for lossy media includes a questionable step for the TE_z case, which will be discussed in further detail in Section IV. Furthermore, their TF/SF boundary extends into the upper and lower PML regions, which makes obtaining the far field with a near-field-to-far-field transform (NFFFT) impractical.

Neither of the above studies addresses vital issues such as the placement of the field variables, stability assessment, excitation techniques, etc. The issue of instability, which is encountered for large incidence angles, is an especially important one. In this paper, we present a complete development of the plane-wave injector for general layered media by carefully assessing these issues. Our derivation also differs from that of Yi *et al.* [4] in that it lends itself naturally to generalization to other types of dispersive media.

Finally, neither of the techniques described above considers the presence of *inhomogeneous* or *evanescent plane waves* [6]. Our proposed plane-wave injector has the capability of handling *narrowband* inhomogeneous plane waves as an extension of its traditional function of injecting homogeneous plane waves. The reasons for the assumption of a narrowband spectrum will be made clear in a later section.

Compared to previous plane-wave injectors, the formulation introduced in this paper provides another key advantage: the

Manuscript received February 20, 2007; revised July 2, 2007. This work was supported in part by the John Pippin Chair in Electromagnetics within the School of Electrical and Computer Engineering, Georgia Institute of Technology.

İ. R. Çapoğlu was with the School of Electrical and Computer Engineering, Georgia Institute of Technology, Atlanta, GA 30332-0250 USA. He is now with the Biomedical Engineering Department, Northwestern University, Evanston, IL 60208-3100 USA (e-mail: capoglu@ieee.org).

G. S. Smith is with the School of Electrical and Computer Engineering, Georgia Institute of Technology, Atlanta, GA 30332-0250 USA (e-mail: glenn.smith@ece.gatech.edu).

Digital Object Identifier 10.1109/TAP.2007.913088

0018-926X/$25.00 © 2008 IEEE

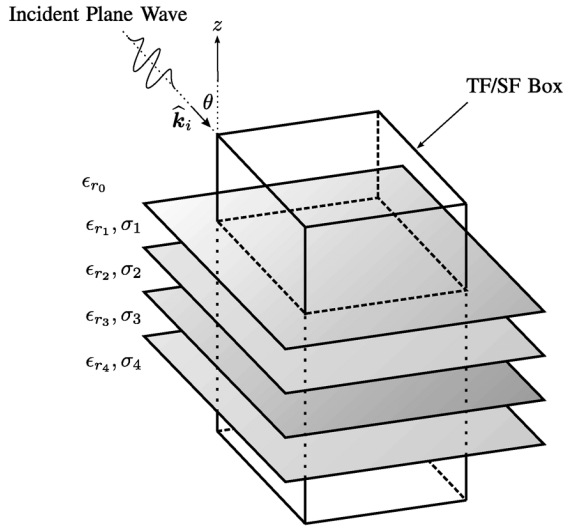

Fig. 1. Geometry of the plane-wave injector for general layered media.

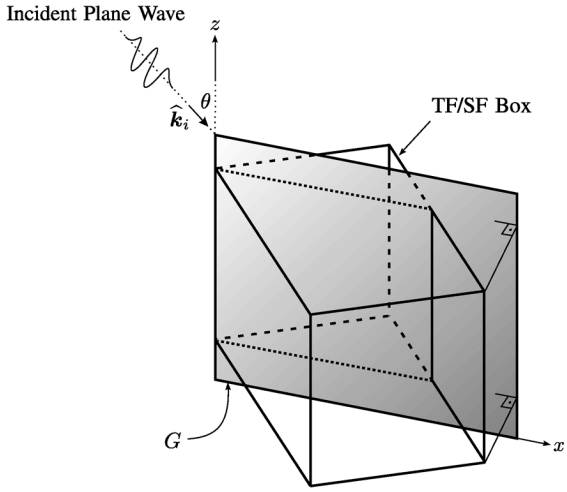

Fig. 2. Principal plane G for the incident plane wave.

possibility of incorporating the NFFFT into the FDTD analysis of scattering problems. This is because the proposed TF/SF boundary does not penetrate into the PML layer, and therefore, it can be enclosed by a NFFFT surface. For example, the plane-wave injector described here can be easily used together with the NFFFT that was developed for the grounded dielectric slab [7], [8].

The rest of the paper is organized as follows. In Section II , the geometry of the problem is presented. In Section III, the TF/SF plane-wave injector is developed for lossless layered media. In Section IV, the plane-wave injector is generalized to lossy layered media. In Section V , the plane-wave injector is generalized to include narrowband inhomogeneous plane waves. Illustrative examples are presented throughout the development. In Section VI, we present a summary of our study.

II. Geometry

A planar layered (or multilayered) medium is characterized by the invariance of material properties in planes perpendicular to an axis called the axis of symmetry. In our treatment of layered media, we confine ourselves to permittivity and conductivity variations along the axis of symmetry. The results for permeability variations follow either from similar analysis, or duality arguments. We restrict the uppermost and lowermost layers to half spaces with constant permittivity and conductivity (a perfectly-conducting half space is allowed for the lowermost layer). We also assume that the material properties ϵ_{r_n}, σ_n are independent of frequency, i.e., the only sources of dispersion are the frequency-independent conductivities of the layers.

The geometry for the TF/SF plane-wave injector is shown in Fig. 1 for a five-layer medium. The TF/SF boundary is denoted by the rectangular prism that passes through the entire layered structure in Fig. 1. The axis of symmetry is z, and the planar interfaces between the layers are represented by sheets with different shades of gray. The layers between the interfaces have permittivities ϵ_{r_n} and conductivities σ_n, for $n = 0 \ldots 4$. The uppermost layer is assumed to be lossless ($\sigma_0 = 0$), which is justified by the need for a well-defined wavefront for the incoming plane wave that does not disperse until it makes contact with the dielectric layers. This wavefront is denoted by the wavy arrow in Fig. 1 .

In the following sections, we will describe the method for obtaining the field values of the incident plane wave on the TF/SF box in Fig. 1.

III. Solving for the Incident Field

A. Formulation

The first step in solving for any electromagnetic field is to observe the symmetries inherent in the geometry and the excitation. The most obvious symmetry in the plane-wave injector setting in Fig. 1 is the invariance of both the geometry and the incident plane wave in a direction that is perpendicular to a plane called the *principal plane*, represented by the gray sheet G in Fig. 2. Without loss of generality, we assume that G coincides with the xz plane, so there is no variation in the y direction. This plane contains both the direction of propagation $\hat{\boldsymbol{k}}_i$ for the incident wave and the axis of symmetry z for the layered medium. From the aforementioned symmetry, it follows that the incident plane wave at any point in space can be obtained by projection onto G. In the following analysis, we will therefore be concerned with the solution of the incident field on the two-dimensional plane G.

The preceding simplification to two dimensions is by no means unique to the plane wave. In fact, it is valid for any two-dimensional source, an example of which is an infinite current filament with uniform current perpendicular to the principal plane G in Fig. 2. Owing to its relative simplicity, it is possible to find much deeper symmetries for the plane wave, which allows further simplification to one dimension. This reduction is explained next.

At every interface in the layered structure, the component of the phase velocity tangential to the interface (x component) must be the same. If c_0 is the speed of light in the lossless uppermost medium ($n = 0$), then $v_{p_x} = c_0 / \sin\theta$ in all layers, where θ is the angle between $\hat{\boldsymbol{k}}_i$ and $\hat{\boldsymbol{z}}$, see Fig. 2. This statement is equivalent to what is called *phase matching* in frequency domain. Now any component of the electromagnetic field in any

layer can be written as a function of only two variables: z and $t - x/v_{p_x} = t - x\sin\theta/c_0$. Thus the partial derivatives with respect to time and with respect to the spatial variable x are simply related. After using this relationship for derivatives and the invariance with respect to y, Maxwell's equations can be split into two independent sets; the details are given in [8]. The first set of equations has only one component to the electric field, $\mathcal{E}_y$, and this component is perpendicular to the plane G, so this set of equations is referred to as *transverse electric* (TE). After introducing the notation $\mathcal{E}^h = \mathcal{E}_y$, $\mathcal{H}^h = -\mathcal{H}_x$, this set of equations becomes

$$\begin{aligned}\frac{\partial \mathcal{E}^h}{\partial z} &= -[\mu_0]\frac{\partial \mathcal{H}^h}{\partial t}\\ \frac{\partial \mathcal{H}^h}{\partial z} &= -\left[\epsilon_0\left(\epsilon_r - \epsilon_{r_0}\sin^2\theta\right)\right]\frac{\partial \mathcal{E}^h}{\partial t} \qquad \text{(TE)}\\ \mathcal{H}_z &= Y_0\sqrt{\epsilon_{r_0}}\sin\theta\,\mathcal{E}^h. \qquad (1)\end{aligned}$$

The second set of equations has only one component to the magnetic field, $\mathcal{H}_y$, and this component is perpendicular to the plane G, so this set of equations is referred to as *transverse magnetic* (TM). After introducing the notation $\mathcal{E}^e = \mathcal{E}_x$, $\mathcal{H}^e = \mathcal{H}_y$, this set of equations becomes

$$\begin{aligned}\frac{\partial \mathcal{E}^e}{\partial z} &= -\left[\frac{\mu_0\left(\epsilon_r - \epsilon_{r_0}\sin^2\theta\right)}{\epsilon_r}\right]\frac{\partial \mathcal{H}^e}{\partial t}\\ \frac{\partial \mathcal{H}^e}{\partial z} &= -[\epsilon_0\epsilon_r]\frac{\partial \mathcal{E}^e}{\partial t} \qquad \text{(TM)}\\ \mathcal{E}_z &= -\frac{Z_0\sqrt{\epsilon_{r_0}}\sin\theta}{\epsilon_r}\,\mathcal{H}^e. \qquad (2)\end{aligned}$$

In (1) and (2), ϵ_r and ϵ_{r_0} denote the relative permittivities at the field position and the uppermost layer, respectively, and $Z_0 = 1/Y_0 = (\mu_0/\epsilon_0)^{1/2}$. For simplicity, it is assumed that there is no loss, i.e., the relative permittivity ϵ_r is real. The results will be generalized to lossy media in the following section.

The behavior of the incident field, which consists of the initial plane wave incident from the uppermost layer and all of the reflections at the interfaces, is completely described by the first two equations in each set, (1) and (2). Notice that they are the familiar transmission-line (TL) equations for propagation in the direction z, and that they only involve components of the field that are transverse to z: $\mathcal{E}^h, \mathcal{H}^h$ for TE and $\mathcal{E}^e, \mathcal{H}^e$ for TM. These equations must be discretized for use in the FDTD method. As will be seen shortly, the discretized field components are placed on a 1-D *auxiliary grid*, similar to the one used in the free-space TF/SF method [1]. Unlike the free-space auxiliary grid, our grid always aligns with the z axis, since (1) and (2) describe the evolution of the fields in the z direction.

The first two equations in (1) closely resemble the equations for a 1-D TEM wave [1], which suggests the staggered temporal-spatial positioning of $\{\mathcal{E}^h, \mathcal{H}^h\}$, along with leap-frog time updating. The third equation in (1) suggests placing $\mathcal{H}_z$ at the same spatial positions as $\mathcal{E}^h$. However, since all the components of the electric field in the main simulation grid are usually discretized identically in time, we choose to evaluate $\mathcal{H}_z$ at the same time points as $\{\mathcal{H}^e, \mathcal{H}^h\}$. This has the slight disadvantage of having to interpolate $\mathcal{H}_z$ in time for the discretization of the third equation in (1). The preceding arguments apply similarly to the equations in (2). The resulting placement of the field components $\{\mathcal{E}^h, \mathcal{E}^e, \mathcal{E}_z, \mathcal{H}^h, \mathcal{H}^e, \mathcal{H}_z\}$ on the temporal-spatial 1-D auxiliary grid is shown in Fig. 3(a). The update equations are given by the discretization of (1) and (2)

$$\mathcal{H}^h|_{k+1/2}^{n+1/2} = \mathcal{H}^h|_{k+1/2}^{n-1/2} - \frac{\Delta t}{\mu_0 \Delta z}\left[\mathcal{E}^h|_{k+1}^n - \mathcal{E}^h|_k^n\right] \qquad (3)$$

$$\mathcal{E}^h|_k^{n+1} = \mathcal{E}^h|_k^n - \frac{\Delta t}{\epsilon_0\left(\epsilon_r|_k - \epsilon_{r_0}\sin^2\theta\right)\Delta z} \cdot \left[\mathcal{H}^h|_{k+1/2}^{n+1/2} - \mathcal{H}^h|_{k-1/2}^{n+1/2}\right] \qquad (4)$$

$$\mathcal{H}_z|_k^{n+1/2} = -\mathcal{H}_z|_k^{n-1/2} + 2Y_0\sqrt{\epsilon_{r_0}}\sin\theta\,\mathcal{E}^h|_k^n \qquad (5)$$

and

$$\mathcal{H}^e|_{k+1/2}^{n+1/2} = \mathcal{H}^e|_{k+1/2}^{n-1/2} - \frac{\epsilon_r|_{k+1/2}\Delta t}{\mu_0\left(\epsilon_r|_{k+1/2} - \epsilon_{r_0}\sin^2\theta\right)\Delta z} \cdot \left[\mathcal{E}^e|_{k+1}^n - \mathcal{E}^e|_k^n\right] \qquad (6)$$

$$\mathcal{E}^e|_k^{n+1} = \mathcal{E}^e|_k^n - \frac{\Delta t}{\epsilon_0\epsilon_r|_k \Delta z}\left[\mathcal{H}^e|_{k+1/2}^{n+1/2} - \mathcal{H}^e|_{k-1/2}^{n+1/2}\right] \qquad (7)$$

$$\mathcal{E}_z|_{k+1/2}^{n+1} = -\mathcal{E}_z|_{k+1/2}^n - \frac{2Z_0\sqrt{\epsilon_{r_0}}\sin\theta}{\epsilon_r|_{k+1/2}}\mathcal{H}^e|_{k+1/2}^{n+1/2}. \qquad (8)$$

Note that the field components $\{\mathcal{E}^h, \mathcal{E}^e, \mathcal{H}_z\}$ are evaluated at integer spatial positions $(k, k+1, \ldots)$ and the field components $\{\mathcal{H}^h, \mathcal{H}^e, \mathcal{E}_z\}$ are evaluated at half-integer spatial positions $(k-1/2, k+1/2, \ldots)$, consistent with the placement in Fig. 3(a). The relative permittivity ϵ_r is evaluated at either integer (k) or half-integer $(k+1/2)$ positions. At the integer positions (k), the permittivity values at the locations of $\mathcal{E}_x, \mathcal{E}_y$ are used, whereas for the half-integer positions $(k+1/2)$, the permittivity values at the locations of $\mathcal{E}_z$ are used. Near the dielectric interfaces, equivalent permittivities [9], [10] are used to preserve second-order accuracy. Changes in the relative permittivity $\epsilon_r|_k$ resulting from material discontinuities create reflections, which represent the reflections of the incident plane wave from the dielectric interfaces.

Now, the evolution of the incident electric and magnetic field components are completely described in the z direction by the TE and TM equation sets (1) and (2), given the incident field is a plane wave. This evolution is approximated by central differences in the 1-D auxiliary grid in Fig. 3(a). We have seen that the phase velocity in the x direction is constant $(c_0/\sin\theta)$ in all layers; therefore, fields at different x values can be easily derived from those at any other x value by introducing a time delay. This property can be used to obtain the field values on the *two-dimensional* principal plane G, as shown in Fig. 3(b). A 1-D auxiliary grid as in Fig. 3(a) is placed at $x = 0$; this is shown magnified in the figure. Because only the spatial placement is shown, the field components $\{\mathcal{E}^h, \mathcal{E}^e, \mathcal{H}_z\}$ and $\{\mathcal{H}^h, \mathcal{H}^e, \mathcal{E}_z\}$ are collated at the same position (index k) on the z axis. Once the time history of the 1-D auxiliary grid at $x = 0$ is determined using the update equations (3)–(8), the field values at other x values can be simply obtained by introducing a time delay. For example, the TE electric field component $\mathcal{E}^h$ at $x = x_0$ is given by the value of $\mathcal{E}^h$ at $x = 0$ at an earlier time [see Fig. 3(b)]

$$\begin{aligned}\mathcal{E}^h(x_0, z, t) &= \mathcal{E}^h(0, z, t-\tau)\\ &= \mathcal{E}^h\left(0, z, t - \frac{x_0\sin\theta}{c_0}\right). \qquad (9)\end{aligned}$$

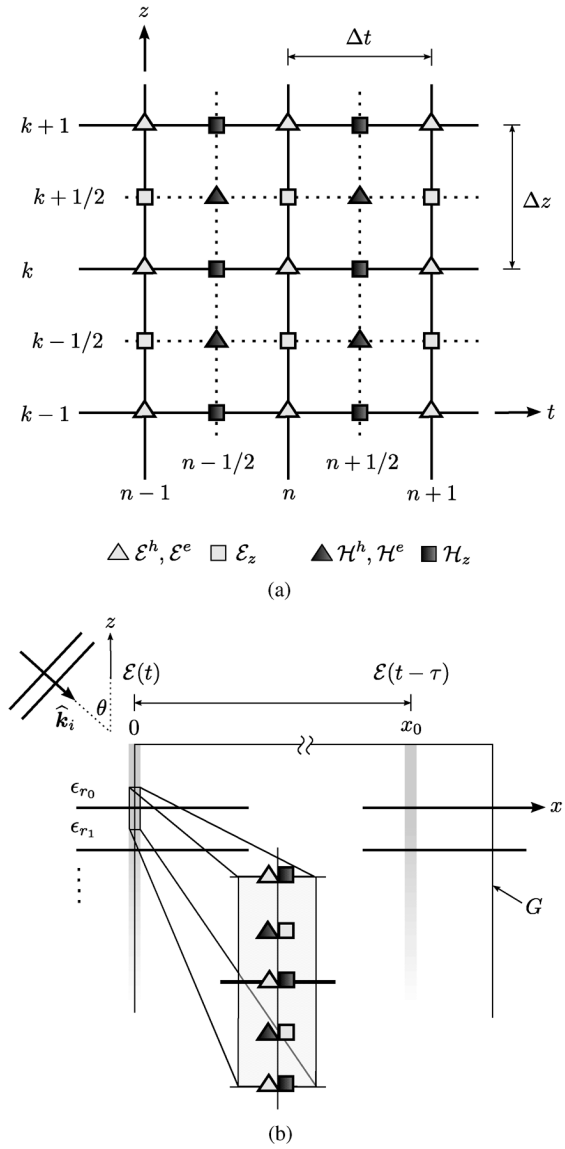

Fig. 3. Usage of the 1-D auxiliary grid for obtaining the incident field on the principal plane G. (a) The temporal-spatial 1-D auxiliary grid. (b) The 2-D principal plane G, with a 1-D auxiliary grid at $x = 0$.

In light of the above discussion, the method of obtaining the incident field values on the TF/SF box in Fig. 1 can be summarized as follows. The time history of a single 1-D auxiliary grid at $x = 0$ is computed using the update equations (3)–(8), and stored offline. When an incident field value is required at any point on the TF/SF box within the main simulation, the point is projected onto the principal plane G, and the field value at the projected point on G is calculated using the available information on the time history at $x = 0$, along with the time delay relation (9). Because the time history consists of a discrete set of time values, interpolation in time is usually necessary while using (9).

B. Stability, Excitation and Dispersion

We now have the necessary tools to compute the incident field on the principal plane G, which consists of the initial plane wave

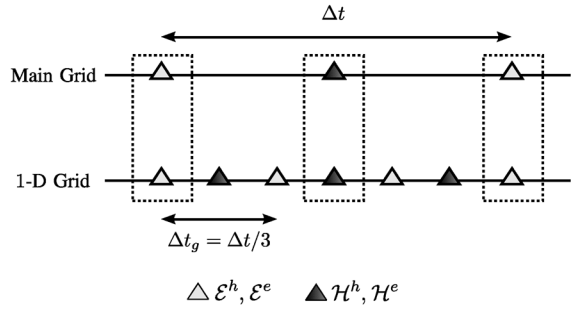

Fig. 4. The reduction of the time step in the 1-D auxiliary grid for stability.

incident from the uppermost layer and all of the reflections from the dielectric interfaces. There are, however, two more aspects of the 1-D auxiliary grid in Fig. 3(a) that require further elaboration. First, we need to investigate the important issue of stability in the 1-D auxiliary grid. The stability requirement for (3) and (4) and (6) and (7) is given by the Courant stability criterion

$$\Delta t \leq \frac{\Delta z}{c'} \tag{10}$$

in which $c' = (\epsilon_0 \mu_0 (\epsilon_r - \epsilon_{r_0} \sin^2 \theta))^{-1/2}$ is the velocity of propagation in the 1-D auxiliary grid in Fig. 3(a). Because it is possible to have $c' > c = (\epsilon_0 \mu_0)^{-1/2}$, the use of the same values $\Delta t, \Delta z$ in the 1-D auxiliary grid as in the main grid might lead to instability. In this case, it is necessary to use either a larger Δz or a smaller Δt for the 1-D auxiliary grid. The former is undesirable because it results in poor spatial accuracy. Hence, a smaller time step, $\Delta t_g = \Delta t/k$ $(k > 1)$, is used in the 1-D auxiliary grid to maintain stability. Because it is still necessary to conform to the main-grid time spacing, Δt is divided by increasing *odd* integer values $(k = 3, 5, \ldots)$, as θ is increased further beyond the stability limit. In these cases, k 1-D-auxiliary-grid updates are done in a single main grid update cycle. An example with $k = 3$ is shown in Fig. 4, in which the upper line denotes the time axis for the main grid and the lower line denotes the time axis for the 1-D auxiliary grid. It is seen that the choice of odd k guarantees that every field component in the main grid has a corresponding field component in the 1-D auxiliary grid at the same instant of time. This correspondence is shown by the dashed rectangles in Fig. 4.

The second issue to consider is the *excitation* of the 1-D auxiliary grid, which consists of two parts: the introduction of the initial plane wave [shown in the top left corner in Fig. 3(b)], and the absorption of the scattered and transmitted plane waves at the two ends of the grid, namely, the proper termination of the grid. These two parts are shown schematically in Fig. 5. For introducing the initial plane wave, a one-dimensional TF/SF boundary [1] is constructed. Corrections are applied to the update equations (3)–(8) for two field components (one $\mathcal{E}$ and one $\mathcal{H}$) situated at opposite sides of the TF/SF boundary. The correction terms are directly proportional to the h- or e-polarized components of the initial plane wave. Exact expressions for these terms can be found in [1]. At the lower and upper ends of the grid, absorbing boundary conditions (ABC) are applied to

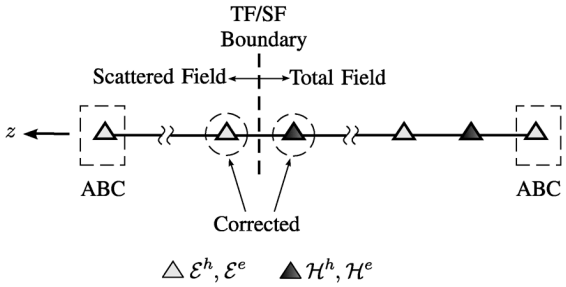

Fig. 5. Grid termination and incident wave conditions for the 1-D auxiliary grid.

efficiently absorb the waves that reach these points. A simple first-order ABC is sufficient for most practical purposes

$$\mathcal{F}_0^{n+1} = \mathcal{F}_0^n + \frac{S-1}{S+1}\left(\mathcal{F}_1^{n+1} - \mathcal{F}_0^n\right) \tag{11}$$

$$\mathcal{F}_{N+1}^{n+1} = \mathcal{F}_N^n + \frac{S-1}{S+1}\left(\mathcal{F}_N^{n+1} - \mathcal{F}_{N+1}^n\right) \tag{12}$$

in which $\mathcal{F}$ is $\mathcal{E}^e$ or $\mathcal{E}^h$, $S = c'\Delta t/\Delta z$ is the Courant number, and N is the number of grid cells in the 1-D auxiliary grid.

Finally, we need to quantify the effects of *grid dispersion* on the performance of the plane-wave injector. In our plane-wave injector, the incident field is obtained through the use of a 1-D auxiliary grid, which is inherently dispersive. This turns out to be an advantage, since the dispersion effects in the 3-D grid can be emulated by the dispersion in the 1-D auxiliary grid, resulting in a more accurate incident field [5]. For our purposes, the dispersion analysis for the 2-D grid in [5] must be extended to the 3-D grid, since the principal plane in Fig. 2 need not be parallel to one of the principal axes. Specifically, we need to consider the difference between the dispersion factors in the 3-D main grid and the 1-D auxiliary grid. The details of this procedure can be found in [8]. In summary, it is found that the discrepancy between the dispersion factor γ_{3D} in the 3-D main grid and the dispersion factor γ_{1D} in the 1-D auxiliary grid is maximum for $\phi = 45°$, and this maximum is 25% greater than the value for $\phi = 0$, assuming 10 cells per free-space wavelength. The results are virtually independent of the Courant factor.

C. Example

We will now present an example that illustrates the use of the plane-wave injector described in the previous subsections. The geometry for the example is shown in Fig. 6(a): two parallel infinite dielectric slabs with relative permittivity $\epsilon_r = 2.5$, thickness 5 cm, and spacing 5 cm are in free space. They are illuminated by an incident plane wave with direction of propagation $\hat{\boldsymbol{k}}_i$ lying in the xz plane at an angle of $\theta = 70°$ to the z axis. The electric field of this wave is transverse to $\hat{\boldsymbol{k}}_i$ at an angle of 45° to the y axis, and it is a unit-amplitude Gaussian pulse in time: $\mathcal{E}^i(t) = \exp(-((t-t_0)/\tau)^2/2)$ with $\tau = 40$ ps and $t_0 = 6\tau$.

The parameters for the FDTD simulation are grid size 50 cm × 1 cm × 50 cm, grid spacing $\Delta x = \Delta y = \Delta z = \Delta = 1$ mm, and time step $\Delta t = (0.98/\sqrt{3})\Delta/c$. The solution space is surrounded by convolutional PML [11] of thickness 0.5 cm, with the slabs penetrating into the PML. The TF/SF boundary,

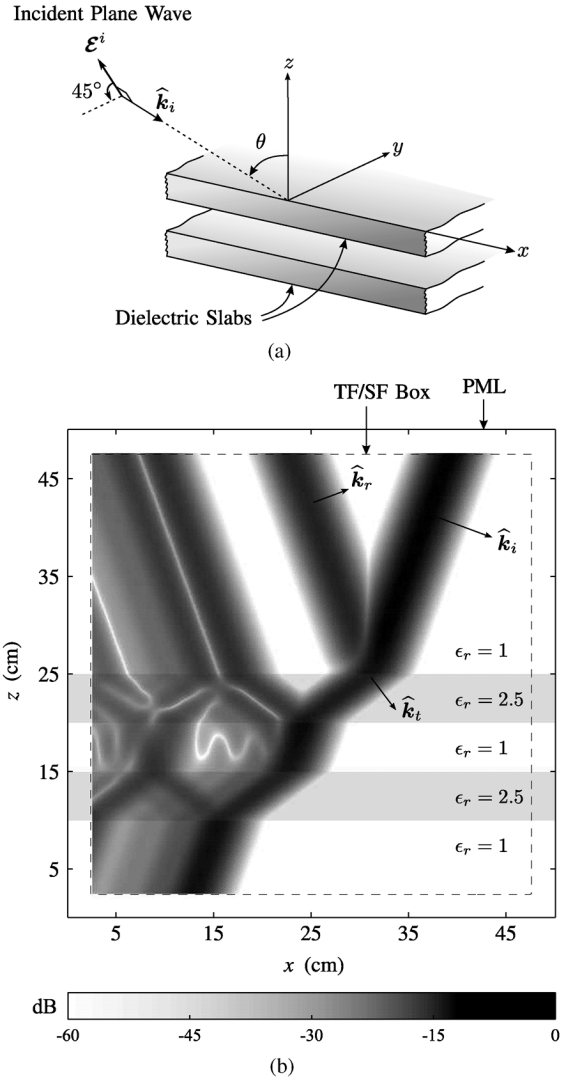

Fig. 6. An example of plane-wave injection into a layered FDTD grid. (a) Geometry. (b) Grayscale plot for the dB-magnitude of the electric field in the xz plane.

represented by the dashed rectangle in Fig. 6(b), is 2.5 cm from the PML boundaries. To satisfy the stability requirement discussed earlier, the time step for the 1-D auxiliary grid is chosen to be one third of that for the main grid: $\Delta t_g = \Delta t/3$.

In Fig. 6(b), the magnitude of the electric field on the xz plane is displayed in dB on a gray scale, with black representing 0 dB and white representing −60 dB. To help with interpretation, the directions of propagation for the initial plane wave, $\hat{\boldsymbol{k}}_i$, and the first reflection and transmission at the upper surface of the top slab, $\hat{\boldsymbol{k}}_r$ and $\hat{\boldsymbol{k}}_t$, are shown on the plot. The multiple reflections from and transmissions through the two slabs are evident in the plot. Notice that, as expected, there is no field in the region between the TF/SF box and the PML. If an additional object were to be placed in the solution space, for example in one of the slabs, the scattered field from this object would appear in this region. If the scattered far field from the object were desired, it could be obtained by applying a near-field-to-far-field transformer for layered media to the field in this region (such a transformer is presented in [8]). Note that this far field would only

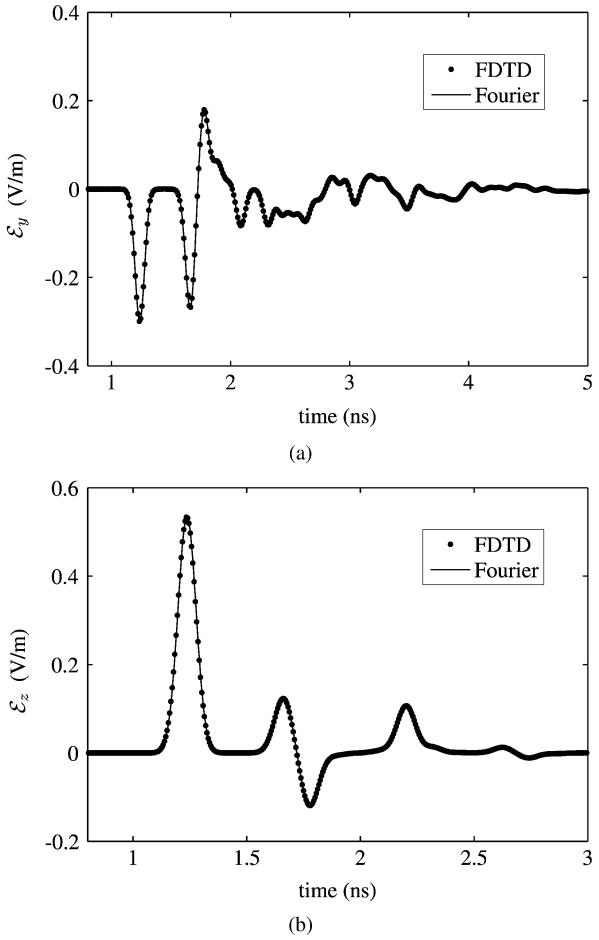

Fig. 7. Comparison of the components of the electric field at the center of Fig. 6(b) obtained through the FDTD method (dots) and Fourier transformation (solid line): (a) y component, (b) z component.

be due to the object in the presence of the slabs; it would not include the plane-wave scattering from the slabs.

Before concluding this section, we will compare the results given in the above example to those obtained using frequency-domain analysis followed by inverse Fourier transformation. The frequency-domain analysis of plane waves obliquely incident on layered media is well-documented in the literature [12]. Computational routines are also available online [13]. In Fig. 7, the y and z components of the electric field at the center of the FDTD grid in Fig. 6(b) are compared with those obtained using frequency-domain analysis and inverse Fourier transformation. The two results are seen to be in very good agreement. More quantitatively, the differences are less than 0.7% of the peak value at all points for both cases.

IV. Generalization to Lossy Media

A. Formulation

The time-domain and frequency-domain derivations of the transmission-line equations (1) and (2) are given in [8] and [14], respectively, for lossless layered media. We can find time-domain transmission-line equations similar to (1) and (2) for lossy layered media, but the direct time-domain route followed in [8] turns out to be inefficient. Instead, we will start with the frequency-domain versions of (1) and (2) given in [14], and try to invert these equations to the time domain in the presence of loss. One advantage of this detour is that it allows easier comparison of our results with those in an earlier study [5], in which the same procedure is followed. Another advantage is the possibility of representing loss directly by using the *complex relative permittivity* ϵ_r^*

$$\epsilon_r^* = \epsilon_r' - j\frac{\sigma}{\omega\epsilon_0} \tag{13}$$

in which σ is the conductivity (S/m) of the material and ω is the angular frequency. The frequency-domain transmission-line equations in [14] are

$$\begin{aligned} \frac{\partial E^h}{\partial z} &= -j\omega\mu_0 H^h \\ \frac{\partial H^h}{\partial z} &= -j\omega\epsilon_0\left(\epsilon_r^* - \epsilon_{r_0}\sin^2\theta\right)E^h \qquad \text{(TE)} \\ H_z &= Y_0\sqrt{\epsilon_{r_0}}\sin\theta\, E^h \end{aligned} \tag{14}$$

and

$$\begin{aligned} \frac{\partial E^e}{\partial z} &= -j\omega\frac{\mu_0\left(\epsilon_r^* - \epsilon_{r_0}\sin^2\theta\right)}{\epsilon_r^*}H^e \\ \frac{\partial H^e}{\partial z} &= -j\omega\epsilon_0\epsilon_r^* E^e \qquad \text{(TM)} \\ E_z &= -\frac{Z_0\sqrt{\epsilon_{r_0}}\sin\theta}{\epsilon_r^*}H^e \end{aligned} \tag{15}$$

in which Roman font denotes frequency-domain variables. For no loss ($\sigma = 0$), these equations yield the time-domain transmission-line equations (1) and (2) upon inverse Fourier transformation ($j\omega \to \partial/\partial t$). However, if there is loss in the medium, the complex ϵ_r^* term in the denominator of the first TM equation in (15) complicates its direct inversion to the time domain. In [5], ϵ_r^* is carried inside the partial derivative $\partial/\partial z$ in the left-hand side and another variable $E^{e'}$ is defined for $\epsilon_r^* E^e$. The accuracy of this step is questionable for the following reason: From the TM equations in (15), it can be shown that both E^e and H^e must be continuous throughout the medium. Therefore, $E^{e'} = \epsilon_r^* E^e$ must be *discontinuous* across a material boundary. This discontinuity poses a problem when we attempt to discretize $E^{e'}$ and approximate $\partial E^{e'}/\partial z$ by the resulting finite differences. Because the theoretical values for $E^{e'}$ are discontinuous, the finite difference approximation of $\partial E^{e'}/\partial z$ predicts unnatural spikes in the H-field, although the H-field is continuous in theory. To avoid this problem, we will use a different approach. We will let

$$H^{e'} = \frac{H^e}{\epsilon_r^*} \tag{16}$$

and invert (14) and (15) to the time domain using this definition

$$\begin{aligned} \frac{\partial \mathcal{E}^h}{\partial z} &= -\mu_0\frac{\partial \mathcal{H}^h}{\partial t} \\ \frac{\partial \mathcal{H}^h}{\partial z} &= -\sigma\mathcal{E}^h - \epsilon_0\left(\epsilon_r' - \epsilon_{r_0}\sin^2\theta\right)\frac{\partial \mathcal{E}^h}{\partial t} \qquad \text{(TE)} \\ \mathcal{H}_z &= Y_0\sqrt{\epsilon_{r_0}}\sin\theta\,\mathcal{E}^h \end{aligned} \tag{17}$$

and

$$\frac{\partial \mathcal{E}^e}{\partial z} = -\frac{\sigma\mu_0}{\epsilon_0}\mathcal{H}^{e'} - \mu_0\left(\epsilon_r' - \epsilon_{r_0}\sin^2\theta\right)\frac{\partial \mathcal{H}^{e'}}{\partial t}$$
$$\frac{\partial \mathcal{H}^e}{\partial z} = -\sigma\mathcal{E}^e - \epsilon_0\epsilon_r'\frac{\partial \mathcal{E}^e}{\partial t} \qquad \text{(TM)}$$
$$\mathcal{E}_z = -Z_0\sqrt{\epsilon_{r_0}}\sin\theta\,\mathcal{H}^{e'}. \qquad (18)$$

In addition to the above equations, (16) introduces another equation that defines the relation between the auxiliary variable $\mathcal{H}^{e'}$ and the magnetic field variable $\mathcal{H}^e$

$$\frac{\partial \mathcal{H}^e}{\partial t} = \frac{\sigma}{\epsilon_0}\mathcal{H}^{e'} + \epsilon_r'\frac{\partial \mathcal{H}^{e'}}{\partial t}. \qquad (19)$$

Now, the reason for defining $H^{e'} = H^e/\epsilon_r^*$ instead of $E^{e'} = \epsilon_r^* E^e$ is clear: The spatial derivative of $\mathcal{H}^{e'}$ never appears in (18) and (19), so the discontinuity of $\mathcal{H}^{e'}$ across material boundaries does not affect the finite-difference approximation. The validity of this assertion will be demonstrated through an example in the next subsection.

The discretization of the TE and TM equations in (17) and (18) lead to familiar update equations, the common forms of which can be found in [1]. The update equation corresponding to the auxiliary equation (19) has the same form. This auxiliary update converts $\mathcal{H}^{e'}$ to $\mathcal{H}^e$ and must be performed together with the first update in (18).

The presence of loss introduces an additional memory requirement for storing the auxiliary variable $\mathcal{H}^{e'}$ and an additional computational requirement for converting $\mathcal{H}^{e'}$ to $\mathcal{H}^e$. Since the 1-D auxiliary grid in Fig. 3(a) is usually much smaller than the main grid, these additional requirements do not cause an appreciable reduction in performance.

Since the uppermost layer is always assumed lossless, the TF/SF boundary and the upper grid termination in Fig. 5 are unchanged when loss is introduced in the other media. However, the presence of loss in the lowermost layer requires a modification in the absorbing boundary condition in (12). A stable method for terminating the finite-difference grid in this case is given in [15].

B. Example

To illustrate the use of the plane-wave injector in lossy layered media, we present a simple and practical example: a two-layered medium consisting of free space and lossy ground. Although the efficiency of the method described above is not affected by the number of layers present in the medium, a two-layered lossy ground is considered merely because of its common appearance in the FDTD literature. The geometry for this example is shown in Fig. 8. The electrical parameters for the ground represented by the gray half-space in Fig. 8 are $\epsilon_r = 2.5$ and $\sigma = 0.5$ S/m, and all of the other parameters for the FDTD simulation, including those for the incident plane wave, are the same as for the example in Fig. 6.

In Fig. 8, the magnitude of the electric field on the xz plane is displayed as before in dB on a gray scale, with black representing 0 dB and white representing -60 dB. Again, to help with interpretation, the directions of propagation for the incident, $\hat{\boldsymbol{k}}_i$, reflected, $\hat{\boldsymbol{k}}_r$, and transmitted, $\hat{\boldsymbol{k}}_t$, waves are shown on the plot. As expected, the transmitted wave is seen to rapidly decay in amplitude after entering the lossy ground. Notice that the shapes of the reflected and transmitted pulses are quite different from the shape of the incident pulse. This is particularly evident for the reflected wave, which is spread out in space much more than the incident wave. This distortion is caused by the frequency dependence of the complex relative permittivity for the ground (13), which not only adds dispersion for the propagation in the ground but also to the reflection coefficient for the wave above the ground.

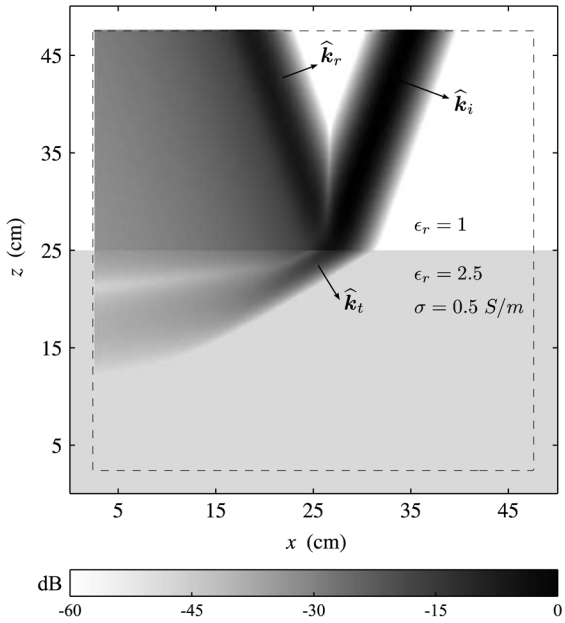

Fig. 8. An example of plane-wave injection into a two-layered FDTD grid representing a lossy ground.

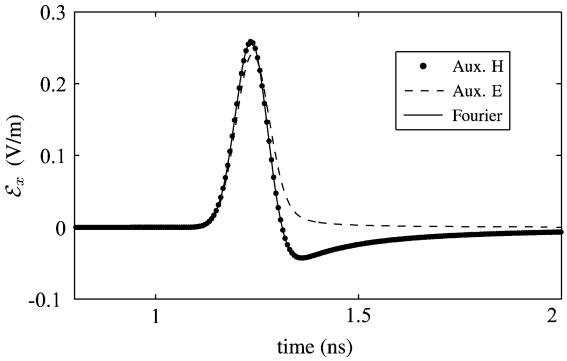

Fig. 9. Comparison of the x components of the electric field at the center of the 1-D auxiliary grid for Fig. 8 obtained through the auxiliary $\mathcal{H}^{e'}$ method (dots), the auxiliary $\mathcal{E}^{e'}$ method (dashed line), and Fourier transformation (solid line).

Finally, we will demonstrate the accuracy of the method introduced above for lossy media by comparing our results to those presented in [5], and those obtained using Fourier transformation [13]. In Fig. 9, we present the x component of the electric field at the center of the 1-D auxiliary grid for Fig. 8 obtained through the auxiliary $\mathcal{H}^{e'}$ method in (16) (dots), the auxiliary $\mathcal{E}^{e'}$ method given in [5] (dashed line), and Fourier transformation (solid line). It is seen that the auxiliary $\mathcal{H}^{e'}$ method is in much better agreement with the Fourier transformation method than the auxiliary $\mathcal{E}^{e'}$ method.

V. Inhomogeneous Plane Waves

A. Formulation

Our treatment so far has excluded a special case, namely, the presence of inhomogeneous (or evanescent) plane waves [6] in certain layers. This type of plane wave is observed in layer n when the incident plane wave is a slow wave for medium n. This means that the transverse phase velocity of the incident plane wave along the interfaces (which is constant throughout the layered medium) is smaller than the speed of light in layer n. In that case, a plane-wave front does not form in the wake of the disturbance at the interface between medium $n-1$ and medium n. For an incidence angle θ and lossless media, the above condition is expressed mathematically as

$$\sin\theta > \sqrt{\frac{\epsilon_{r_n}}{\epsilon_{r_0}}} \tag{20}$$

and called the *total internal reflection* (TIR) condition [12].

Although it is usually considered to be a frequency-domain concept, the inhomogeneous plane wave has a number of distinctive properties in the time domain. Similar to its frequency-domain counterpart, it does not carry any energy in the direction normal to the layers and away from interface (unless there are other layers below for which the TIR condition does not apply), and it decays in amplitude in that direction. Unlike its frequency-domain counterpart, the decay is usually nonexponential. However, as the wave shape becomes more narrowband in frequency, the decay begins to assume the exponential behavior that would be expected from a single-frequency inhomogeneous plane wave.

Perhaps the most peculiar feature an inhomogeneous plane has in the time domain is apparent noncausality [16]. This phenomenon is most evident for signals of wide bandwidth, and is absent for practical narrowband signals in which the spectrum is concentrated about a single frequency. In this section, we adapt the previously described plane-wave injector to include the latter—inhomogeneous plane waves of narrow bandwidth.

The governing transmission-line equations for an inhomogeneous plane wave are the same as the TE and TM equations in (1) and (2) for a homogeneous plane wave; however, the TIR condition in (20) changes the nature of these equations considerably. With the TIR condition, they become

$$\begin{aligned}\frac{\partial \mathcal{E}^h}{\partial z} &= -[\mu_0]\frac{\partial \mathcal{H}^h}{\partial t}\\ \frac{\partial \mathcal{H}^h}{\partial z} &= \left[\epsilon_0\left(\epsilon_{r_0}\sin^2\theta - \epsilon_{r_n}\right)\right]\frac{\partial \mathcal{E}^h}{\partial t}\\ \mathcal{H}_z &= Y_0\sqrt{\epsilon_{r_0}}\sin\theta\,\mathcal{E}^h\end{aligned} \tag{21}$$

and

$$\begin{aligned}\frac{\partial \mathcal{E}^e}{\partial z} &= \left[\frac{\mu_0\left(\epsilon_{r_0}\sin^2\theta - \epsilon_{r_n}\right)}{\epsilon_{r_n}}\right]\frac{\partial \mathcal{H}^e}{\partial t}\\ \frac{\partial \mathcal{H}^e}{\partial z} &= -\left[\epsilon_0\epsilon_{r_n}\right]\frac{\partial \mathcal{E}^e}{\partial t}\\ \mathcal{E}_z &= -\frac{Z_0\sqrt{\epsilon_{r_0}}\sin\theta}{\epsilon_r}\,\mathcal{H}^e\end{aligned} \tag{22}$$

in which the coefficients in square brackets are positive.

If we proceed as we did for the homogeneous plane waves in Section III and discretize (21) and (22) to obtain update equations similar to (3)–(8), we encounter a serious problem: The resulting update equations corresponding to (21) and (22) are *unstable*. In contrast to the TE and TM update equations (3)–(8) for homogeneous plane waves, this instability does not depend on the choice of the time step Δt or the grid spacing Δz. Since (21) and (22) can be written as second-order elliptic equations for $\mathcal{E}^h$ and $\mathcal{E}^e$, the leap-frog algorithm is inherently unstable [17], [18]. If we wish to inject an inhomogeneous plane wave into medium n, we must modify the traditional time-stepping in (3)–(8) to obtain stable solutions of (21) and (22).

Our method relies on the assumption that the system is narrowband; consequently, we shall find it extremely useful to employ the analytic representation (or complex representation) [19] of the narrowband electromagnetic field. This representation is commonly used in the analysis of narrowband disturbances in optics, and is related to the phasor concept used for single-frequency (or monochromatic) systems. In this representation, we regard the field variables as the real parts of complex field variables that are analytic in the complex time plane $\widetilde{t} = t_r + j\,t_i$. For example, the TE electric field variable is written as

$$\mathcal{E}^h(t) = \mathcal{A}(t)\cos(\phi(t) + \omega_0 t) = \Re\{\tilde{\mathcal{E}}^h(t)\} \tag{23}$$

in which ω_0 is the center frequency of the narrowband excitation, and the *analytic TE electric field* is defined as

$$\tilde{\mathcal{E}}^h(t) = \mathcal{E}^h(t) + j\,\hat{\mathcal{E}}^h(t) = \mathcal{A}(t)e^{j\phi(t)}e^{j\omega_0 t}. \tag{24}$$

It can be shown that $\tilde{\mathcal{E}}^h(t)$ is indeed an analytic function [20] in the upper complex half plane $t_i > 0$, and its real and imaginary parts form a Hilbert transform pair [19], [21]

$$\begin{aligned}\mathcal{E}^h &= -\mathfrak{H}\{\hat{\mathcal{E}}^h\}\\ \hat{\mathcal{E}}^h &= \mathfrak{H}\{\mathcal{E}^h\}.\end{aligned} \tag{25}$$

Note that the system of PDEs (21) and (22) is linear and purely real, so the imaginary parts of the analytic field variables can be discarded at the end of the analysis.

The following analysis will be presented for the TE equation set (21); the results are similar for the TM case. The main idea in the analytic representation of narrowband systems is that the functions $\mathcal{A}(t), \phi(t)$ vary slowly compared to $\omega_0 t$, and the derivative of the analytic TE electric variable can be approximated as

$$\frac{\partial \widetilde{\mathcal{E}}^h(t)}{\partial t} \approx (j\omega_0)\mathcal{A}(t)e^{j\phi(t)}e^{j\omega_0 t}. \tag{26}$$

Applying the narrowband assumption (26) to (21), we obtain

$$\mathcal{E}^h = j\,\frac{C}{\omega_0}\frac{\partial \mathcal{H}^h}{\partial z} \tag{27}$$

$$\mathcal{H}^h = j\frac{D}{\omega_0}\frac{\partial \mathcal{E}^h}{\partial z} \tag{28}$$

in which $C = 1/(\epsilon_0(\epsilon_{r_n} - \epsilon_{r_0}\sin^2\theta)) < 0$, and $D = 1/\mu_0 > 0$. For clarity, we have omitted the tilde $(\sim)$ on the field variables; however, it must be understood that the analytic field variables are used throughout the 1-D auxiliary grid whenever there are inhomogeneous waves present in the system. To illustrate the

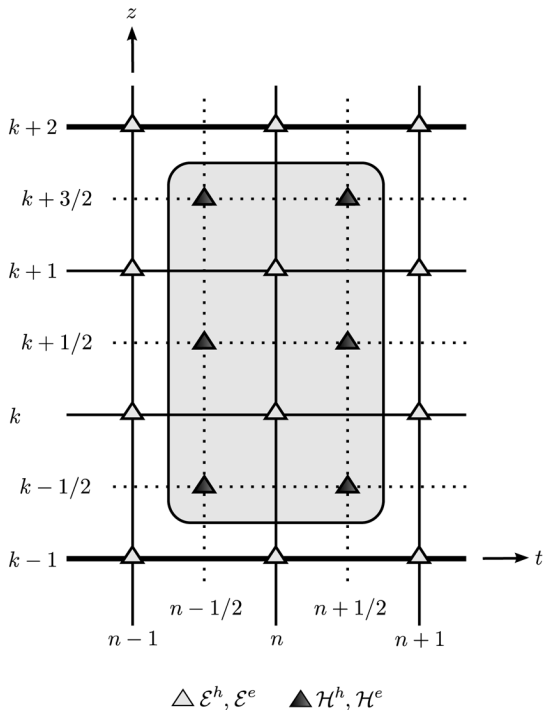

Fig. 10. Grid showing a three-cell thick layer that supports inhomogeneous plane waves.

discretization and the updating method for the above equations, we assume a three-cell thick layer supporting inhomogeneous waves, as shown in Fig. 10. The interfaces between the layer and the neighboring layers are shown by thick solid lines at spatial positions $z = (k+2)\Delta z$ and $z = (k-1)\Delta z$. The plane wave is assumed to be propagating at $z \geq (k+2)\Delta z$ and $z \leq (k-1)\Delta z$. The region in which the plane wave is assumed to be inhomogeneous is enclosed by the gray rectangle in Fig. 10. For the sake of illustration, the rectangle covers only the time values $t = (n-1/2)\Delta t$, $n\Delta t$ and $(n+1/2)\Delta t$, which will appear in our update equations.

In the shaded region in Fig. 10, the TE equations in (27) and (28) can be discretized as follows:

$$\mathcal{E}^h|_k^n = j\frac{C_k}{\omega_0 \Delta z}\left[\frac{\mathcal{H}^h|_{k+1/2}^{n+1/2} + \mathcal{H}^h|_{k+1/2}^{n-1/2}}{2} - \frac{\mathcal{H}^h|_{k-1/2}^{n+1/2} + \mathcal{H}^h|_{k-1/2}^{n-1/2}}{2}\right] \tag{29}$$

$$\frac{\mathcal{H}^h|_{k+1/2}^{n+1/2} + \mathcal{H}^h|_{k+1/2}^{n-1/2}}{2} = j\frac{D_{k+1/2}}{\omega_0 \Delta z}\left[\mathcal{E}^h|_{k+1}^n - \mathcal{E}^h|_k^n\right]. \tag{30}$$

Combining (29) and (30), we obtain the following equation for the TE electric field $\mathcal{E}^h$

$$\mathcal{E}^h|_k^n = \frac{-C_k}{(\omega_0 \Delta z)^2}\left[D_{k+1/2}\mathcal{E}^h|_{k+1}^n - (D_{k+1/2} + D_{k-1/2})\mathcal{E}^h|_k^n + D_{k-1/2}\mathcal{E}^h|_{k-1}^n\right]. \tag{31}$$

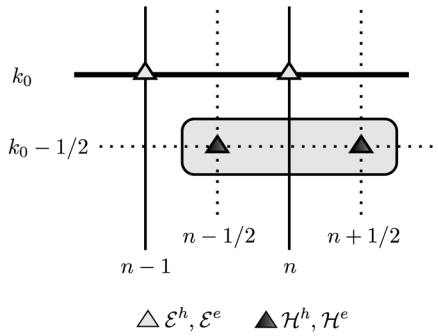

Fig. 11. A simple grid that consists of an isolated interface between two regions with homogeneous (upper) and inhomogeneous (lower) plane waves.

The equation in (31) can be written as a linear tridiagonal system $Ax = b$, for which efficient solution algorithms such as LU decomposition exist [22]. In reference to Fig. 10, the update coefficients $\{D_{k-1/2}, C_k, D_{k+1/2}, C_{k+1}, D_{k+3/2}\}$ are used to fill the 2×2 tridiagonal matrix A, and the update coefficients $\{D_{k-1/2}, C_k, C_{k+1}, D_{k+3/2}\}$ along with $\mathcal{E}_{k+2}^e$, $\mathcal{E}_{k-1}^e$ are used to fill the vector b. After solving for the electric field, the magnetic field can be directly obtained from (30).

It is apparent from (31) that the electric field components in the region with inhomogeneous waves depend on the electric field values at the interfaces, specifically, $\mathcal{E}_{k+2}^h, \mathcal{E}_{k-1}^h$ in Fig. 10. This suggests a straightforward update cycle for the entire 1-D auxiliary grid, which can be summarized as follows. Assuming that the initial values for the electric and magnetic fields are known everywhere in the grid, we start by applying a single leap-frog update to the electric and magnetic field components in the regions with homogeneous waves. Then, we solve for the electric field values in the regions with inhomogeneous waves using the implicit equation (31). Finally, we update the magnetic field values in the same regions using (30).

As a side note, we simply state without detail that if the plane wave is inhomogeneous at the interfaces $(z = (k+2)\Delta z, (k-1)\Delta z$ in Fig. 10), an implicit equation similar to (31) is constructed for the magnetic field $\mathcal{H}^h$, and solved in a similar manner.

B. Stability and Excitation for the 1-D Auxiliary Grid

The updating scheme explained above is unconditionally stable for regions with pure inhomogeneous waves, but the real stability issue arises at the *interfaces*, where a transition from homogeneous plane waves to inhomogeneous plane waves occurs. Some insight can be obtained into this problem by investigating the case shown in Fig. 11, where the 1-D auxiliary grid consists of an isolated interface at $z = k_0\Delta z$ between two regions with homogeneous and inhomogeneous plane waves. At the interface denoted by the thick solid line $(z = k_0\Delta z)$, the plane wave is homogeneous; and right below the interface $(z = (k_0 - 1/2)\Delta z)$, the plane wave is inhomogeneous. All field components except those at $z = k_0\Delta z, (k_0 - 1/2)\Delta z$ are assumed to be zero. Denoting the temporal z-transforms [23] of $\{\mathcal{E}^h|_{k_0}^n, \mathcal{H}^h|_{k_0-1/2}^{n-1/2}\}$ by $\{\tilde{E}, \tilde{H}\}$ respectively, the update equations for the field variables can be written as

$$(z-1)\,\tilde{E} = -\frac{C_{k_0}\Delta t}{\Delta z}\,\tilde{H} \tag{32}$$

$$(z+1)\,\tilde{H} = j\,\frac{2\,D_{k_0-1/2}}{\omega_0 \Delta z}\,\tilde{E}. \tag{33}$$

Note that (32) follows from (4), and (33) follows from (30). This is a mixture of the usual leap-frog scheme used for the homogeneous waves in (3) and (4), and the implicit scheme used for the inhomogeneous waves in (30) and (31). The stability of this mixed update scheme is determined by the roots $z_{1,2}$ of the determinant of the system (32) and (33)

$$z_{1,2} = \pm\sqrt{1-\xi^2} + j\,\xi \tag{34}$$

in which

$$\xi = \frac{C_{k_0} D_{k_0-1/2} \Delta t/\omega_0}{\Delta z^2}. \tag{35}$$

It is readily seen that the roots $z_{1,2}$ stay on the unit circle and the update scheme is stable if and only if

$$\frac{\sqrt{|C_{k_0} D_{k_0-1/2}|}\sqrt{\Delta t/\omega_0}}{\Delta z} < 1. \tag{36}$$

Note that this condition only applies for the simple case for which the 1-D auxiliary grid consists of the close proximity of an interface between two regions with homogeneous and inhomogeneous waves, as shown in Fig. 11. Numerous computer experiments suggest that the stability condition for a more general grid with an arbitrary layered structure has the same form as (36), only with a tighter bound

$$\frac{\sqrt{|C_{k_0} D_{k_0-1/2}|}\sqrt{\Delta t/\omega_0}}{\Delta z} < 0.5. \tag{37}$$

The final stability condition (37) for inhomogeneous plane waves is partly empirical, and presents further challenges for its analytical verification and/or improvement.

Another vital issue that requires attention is the excitation of the 1-D auxiliary grid in the presence of analytic field variables. At this point, we must answer an important question: How do we ensure the analyticity of the field variables throughout the 1-D auxiliary grid? The answer lies in a fundamental result from the theory of partial differential equations (PDEs). The Cauchy-Kowalewski theorem [18] guarantees the analyticity of the field variables if the excitation of the PDEs (21) and (22) governing them is analytic. Remember from the discussion regarding the excitation of the 1-D auxiliary grid in Section III-B (specifically, Fig. 5 and the related discussion) that the corrections applied to the 1-D auxiliary grid are proportional to the initial plane wave, and they play the role of the excitation of the PDEs (21) and (22). Consequently, the critical step in the generalization to analytic field variables is the generalization to an *analytic initial plane wave*. This generalization requires a minor additional computation, i.e., the Hilbert transformation of the real initial plane-wave waveform according to (25). This operation is usually done offline, since the initial plane wave is usually fixed before the simulation.

It should be noted that the generalization to complex field variables doubles the storage and computation requirement in the 1-D auxiliary grid, but this overhead is usually negligible compared to the total computational load of the main simulation.

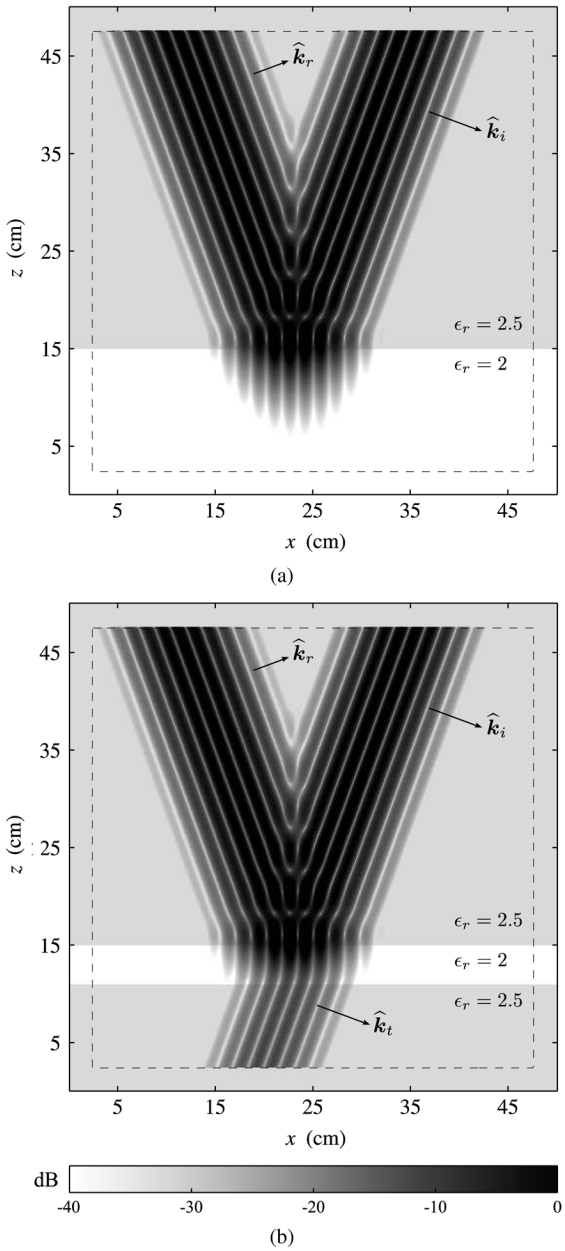

Fig. 12. An example of the injection of narrowband inhomogeneous plane waves into layered media. (a) Total internal reflection. (b) Frustrated total internal reflection. Grayscale plots (decibels) are for the magnitude of the electric field in the xz plane.

C. Example

Finally, we present an example illustrating the creation of narrowband inhomogeneous plane waves using the proposed plane-wave injector. Specifically, we will demonstrate the *frustrated total internal reflection* (FTIR) phenomenon [6], which is inherently associated with inhomogeneous plane waves. The configurations to be used in this discussion are shown in Fig. 12. In Fig. 12(a), a plane wave is incident from a medium with relative permittivity $\epsilon_r = 2.5$ onto a half space with lower permittivity $\epsilon_r = 2$. In Fig. 12(b), the lower half space has been replaced by a slab with $\epsilon_r = 2$ and thickness 4 cm. In both figures, the magnitude of the electric field in the xz plane is displayed as before in dB on a gray scale, with black representing 0 dB and white representing -40 dB.

The electric field of the incident plane wave is a sinusoid of frequency $f_0 = 6.32$ GHz modulated by a unit-amplitude Gaussian pulse: $\mathcal{E}^i(t) = \exp(-((t-t_0)/\tau)^2/2)\sin(2\pi f_0(t-t_0))$ with $\tau = 135$ ps and $t_0 = 6\tau$. This type of waveform is typical for optical signals. As in the other examples, the direction of propagation $\hat{\boldsymbol{k}}_i$ is at the angle $\theta = 70^\circ$ to the z axis. Thus, according to (20), total internal reflection occurs at the interface of the half space: $\sin(\theta) = 0.940 > \sqrt{\epsilon_{r_1}/\epsilon_{r_0}} = \sqrt{2/2.5} = 0.894$. This is evident in the plot for Fig. 12(a). The incident plane wave is completely reflected at the interface, and an inhomogeneous plane wave, which decays in the direction normal to the interface, forms in the lower half space.

The results in Fig. 12(b) are more interesting. Some of the energy in the incident plane wave has been transmitted through the slab and is propagating away from the slab as a plane wave at direction $\hat{\boldsymbol{k}}_t$. The amount of the transmitted energy depends on the thickness of the slab relative to the decay rate for an inhomogeneous plane wave in the slab. This is an example of the FTIR phenomenon mentioned earlier. The transfer of energy from the uppermost layer to the lowermost layer is seemingly in contradiction with the fact that inhomogeneous waves do not carry any energy in the direction normal to the interfaces. However, a thorough analysis shows that this is true for an inhomogeneous wave that forms in a half space and decays in one direction, but not for the sum of two inhomogeneous waves that decay in opposite directions [6].

The FTIR phenomenon summarized in this example is the basis for any technological method that utilizes evanescent waves, such as near-field photolithography [24]–[27], and subwavelength imaging [28]–[30]. Evanescent waves are also frequently used in the FDTD simulations of left-handed metamaterials [28], [27], [31]–[33], which manifest interesting theoretical behavior such as amplification of inhomogeneous plane waves [34]. Since any evanescent field can be expressed as a spectrum of inhomogeneous plane waves, this plane-wave injector has the potential to contribute further toward the better understanding and improvement of such techniques.

VI. Conclusion

In this paper, a TF/SF boundary (or a plane-wave injector) for a general layered medium was presented. Maxwell's equations for a plane wave in a layered medium were reduced to 1-D transmission-line equations on the axis of symmetry, and a 1-D auxiliary FDTD grid was used to solve these equations. Implementation issues such as field placement, stability and excitation were discussed. The plane-wave injector was also generalized to handle narrowband inhomogeneous waves. It was noted that these waves required implicit field updates in their respective regions. Illustrative examples were given throughout the paper to demonstrate the potential of the method.

References

[1] A. Taflove and S. C. Hagness, *Computational Electrodynamics: The Finite-Difference Time-Domain Method*. Boston, MA: Artech House, 2000.

[2] P. Wong, G. Tyler, J. Baron, E. Gurrola, and R. Simpson, "A three-wave FDTD approach to surface scattering with applications to remote sensing of geophysical surfaces," *IEEE Trans. Antennas Propag.*, vol. 44, no. 4, pp. 504–14, Apr. 1996.

[3] T.-T. Hsu and L. Carin, "FDTD analysis of plane-wave diffraction from microwave devices on an infinite dielectric slab," *IEEE Microw. Guided Wave Lett.*, vol. 6, no. 1, pp. 16–18, Jan. 1996.

[4] Y. Yi, B. Chen, D.-G. Fang, and B.-H. Zhou, "A new 2-D FDTD method applied to scattering by infinite objects with oblique incidence," *IEEE Trans. Electromagn. Compat.*, vol. 47, no. 4, pp. 756–62, Nov. 2005.

[5] S. C. Winton, P. Kosmas, and C. M. Rappaport, "FDTD simulation of TE and TM plane waves at nonzero incidence in arbitrary layered media," *IEEE Trans. Antennas Propag.*, vol. 53, no. 5, pp. 1721–1728, May 2005.

[6] G. S. Smith, *An Introduction to Classical Electromagnetic Radiation*. Cambridge, U.K.: Cambridge Univ. Press, 1997.

[7] I. R. Capoglu and G. S. Smith, "A direct time-domain FDTD near-field-to-far-field transform in the presence of an infinite grounded dielectric slab," *IEEE Trans. Antennas Propag.*, vol. 54, no. 12, pp. 3805–14, Dec. 2006.

[8] I. R. Capoglu, "Techniques for Handling Multilayered media in the FDTD method," Ph.D. dissertation, Georgia Institute of Technology, Atlanta, GA, 2007.

[9] T. Hirono, Y. Shibata, W. W. Lui, S. Seki, and Y. Yoshikuni, "The second-order condition for the dielectric interface orthogonal to the Yee-lattice axis in the FDTD scheme," *IEEE Microw. Guided Wave Lett.*, vol. 10, no. 9, pp. 359–61, Sep. 2000.

[10] K.-P. Hwang and A. C. Cangellaris, "Effective permittivities for second-order accurate FDTD equations at dielectric interfaces," *IEEE Microw. Wireless Compon. Lett.*, vol. 11, no. 4, pp. 158–60, Apr. 2001.

[11] J. A. Roden and S. D. Gedney, "Convolution PML (CPML): An efficient FDTD implementation of the CFD-PML for arbitrary media," *Microw. Opt. Technol. Lett.*, vol. 27, no. 5, pp. 334–9, Dec. 2000.

[12] C. A. Balanis, *Advanced Engineering Electromagnetics*. New York: Wiley, 1989.

[13] S. J. Orfanidis, MATLAB toolbox. Electromagnetic Waves and Antennas-Web Resource. Date Accessed: 01/2007 [Online]. Available: http://www.ece.rutgers.edu/~orfanidi/ewa/

[14] K. A. Michalski and J. R. Mosig, "Multilayered media green's functions in integral equation formulations," *IEEE Trans. Antennas Propag.*, vol. 45, no. 3, pp. 508–519, Mar. 1997.

[15] O. Ramadan and A. Y. Niazi, "One way wave equation type ABCs for terminating low loss media," *Electron. Lett.*, vol. 33, no. 24, pp. 2052–4, Nov. 1997.

[16] J. E. Kiwitt and K. Reiss, "Total reflection in the time domain," *Elect. Eng.*, vol. 81, no. 4, pp. 193–8, Nov. 1998.

[17] B. Gustafsson, H. Kreiss, and J. Oliger, *Time Dependent Problems and Difference Methods*. New York: Wiley, 1995.

[18] P. Garabedian, *Partial Differential Equations*. New York: Wiley, 1964.

[19] M. Born and E. Wolf, *Principles of Optics: Electromagnetic Theory of Propagation, Interference and Diffraction of Light*, 7th ed. Cambridge, U.K.: Cambridge Univ. Press, 1999.

[20] J. W. Brown and R. V. Churchill, *Complex Variables and Applications*, 7th ed. New York: McGraw-Hill, 2004.

[21] P. M. Morse and H. Feshbach, *Methods of Theoretical Physics*. New York: McGraw-Hill, 1953.

[22] W. H. Press, B. P. Flannery, S. A. Teukolsky, and W. T. Vetterling, *Numerical Recipes: The Art of Scientific Computing*. Cambridge, U.K.: Cambridge Univ. Press, 1986.

[23] A. V. Oppenheim, R. W. Schafer, and J. R. Buck, *Discrete-Time Signal Processing*, 2nd ed. Upper Saddle River, NJ: Prentice Hall, 1999.

[24] S. Tanaka, M. Nakao, M. Umeda, K. Ito, S. Nakamura, and Y. Hatamura, "Simulation of near-field photolithography using the finite-difference time-domain method," *J. Appl. Phys.*, vol. 89, no. 7, pp. 3547–53, Apr. 2001.

[25] P. Kik, A. Martin, S. Maier, and H. Atwater, "Metal nanoparticle arrays for near-field optical lithography," *Proc. SPIE-Int. Soc. Opt. Eng.*, vol. 4810, pp. 7–13, 2002.

[26] H. Shirasaki and K. Ueta, "Linewidth measurement simulations for semiconductor circuits by scatterometry using the FDTD and the time shortening calculation method," *Proc. SPIE-Int. Soc. Opt. Eng.*, vol. 5375, no. 1, pp. 1331–8, May 2004.

[27] R. Blaikie, D. Melville, and M. Alkaisi, "Super-resolution near-field lithography using planar silver lenses: A review of recent developments," *Microelectron. Eng.*, vol. 83, no. 4–9, pp. 723–9, Apr. 2006.

[28] X. S. Rao and C. K. Ong, "Subwavelength imaging by a left-handed material superlens," *Phys. Rev. E, Stat. Nonlinear Soft Matter Phys.*, vol. 68, no. 6, pp. 67601–1, Dec. 2003.

[29] Q. Zhou, X. Zhu, H. Dai, and E. Pan, "Three-dimensional modeling of near-field imaging in subwavelength periodic structures," *Proc. SPIE-Int. Soc. Opt. Eng.*, vol. 4923, pp. 7–11, 2002.

[30] A. Ono, J. Kato, and S. Kawata, "Subwavelength optical imaging through a metallic nanorod array," *Phys. Rev. Lett.*, vol. 95, no. 26, pp. 267407–1, Dec. 2005.
[31] M. K. Kärkkäinen, "Numerical study of wave propagation in uniaxially anisotropic Lorentzian backward-wave slabs," *Phys. Rev. E, Stat. Nonlinear Soft Matter Phys.*, vol. 68, no. 2, p. 026602, Aug. 2003.
[32] X. S. Rao and C. K. Ong, "Amplification of evanescent waves in a lossy left-handed material slab," *Phys. Rev. B, Condens. Matter Mater. Phys.*, vol. 68, no. 11, pp. 113103–1, Sep. 2003.
[33] A. Alu, N. Engheta, and R. Ziolkowski, "Finite-difference time-domain analysis of the tunneling and growing exponential in a pair of ϵ-negative and μ-negative slabs," *Phys. Rev. E, Stat. Nonlinear Soft Matter Phys.*, vol. 74, no. 1, pp. 16604–1, Jul. 2006.
[34] J. Pendry, "Negative refraction makes a perfect lens," *Phys. Rev. Lett.*, vol. 85, no. 18, pp. 3966–9, Oct. 2000.

İlker R. Çapoğlu (S'02–M'07) received the B.S. degree in electrical and electronics engineering from the Middle East Technical University (METU), Ankara, Turkey, in 2002, and the M.S. and Ph.D. degrees in electrical and computer engineering from the Georgia Institute of Technology, Atlanta, in 2003 and 2007, respectively.

Since September 2007, he has been employed as a Postdoctoral Research Associate in the Biomedical Engineering Department, Northwestern University, Evanston, IL. His research interests include radiation and scattering from spheroidal structures, time-domain multilayered media Green's functions, and the FDTD analysis of multilayered media.

Glenn S. Smith (S'65–M'72–SM'80–F'86) received the B.S.E.E. degree from Tufts University, Medford, MA, in 1967 and the S.M. and Ph.D. degrees in applied physics from Harvard University, Cambridge, MA, in 1968 and 1972, respectively.

From 1972 to 1975, he served as a Postdoctoral Research Fellow at Harvard University and also as a part-time Research Associate and Instructor at Northeastern University, Boston, MA. In 1975, he joined the faculty of the School of Electrical and Computer Engineering at the Georgia Institute of Technology, Atlanta, GA, where he is currently Regents' Professor and John Pippin Chair in Electromagnetics.

He is the author of the book *An Introduction to Classical Electromagnetic Radiation* (Cambridge, 1997) and coauthor of the book *Antennas in Matter: Fundamentals, Theory and Applications* (MIT Press, 1981). He also authored the chapter "Loop Antennas" in the *Antenna Engineering Handbook* (McGraw-Hill, 2007). His technical interests include basic electromagnetic theory and measurements, antennas and wave propagation in materials, and the radiation and reception of pulses by antennas.

Dr. Smith is a member of Tau Beta Pi, Eta Kappa Nu, and Sigma Xi. He is a member of URSI Commissions A and B.